Direct aluminium-alloy upcycling from complete end-of-life vehicles: Supplementary information

P. Krall[1], I. Weißensteiner[2], P. Aster[2], P. Dumitraschkewitz[1], M. A. Tunes[1], T. M. Kremmer[1], S. Samberger[1], B. Trink[3], S. Pogatscher[1].

Supplementary Note 1: Composition scenarios

The three investigated alloys arise from a theoretically calculated composition that would arise from complete melting of the aluminium alloys of three different vehicle types. Their compositions and further a 6016 reference alloy are shown in **Supplementary Table 1**. The basic concept and the results for a low-iron containing last laboratory cooled (60 K/s)-material was presented in our previous work [SR1].

Supplementary Table 1: Chemical composition of the investigated alloys oriented on three different vehicle types. The ELV-mixes are based on today´s average European vehicle (EU), a US pickup-truck (PU) and an electric car (EC) with aluminium representing the balance to 100 % (Bal.).

Alloy	Si [%]	Fe [%]	Cu [%]	Mn [%]	Mg [%]	Zn [%]	Al [%]
EU	5.20	1.20	0.70	0.30	0.75	0.40	Bal.
PU	4.75	1.30	1.30	0.30	0.70	0.50	Bal.
EC	1.50	1.00	0.20	0.30	1.50	0.10	Bal.
6016 Ref	1.06	0.19	0.05	0.06	0.33	0.01	Bal.

Supplementary Note 2: Heat treatment and processing sequences

For the three alloys, different sequences of heat treatment and processing were applied to the as-cast state (CS). This includes homogenizing (H), solution annealing, pre-ageing (PA), natural ageing (NA) and paint-baking (PB). A part of the samples was also pre-strained (PS) to 2 and 5 % plastic deformation. **Supplementary Table 2** gives an overview over the applied parameters, while **Supplementary Figure 1** graphically illustrates the processing ways starting from solution annealing.

Supplementary Table 2: Summary of the applied heat treatments.

Condition	Homo-genising	Solution annealing	Pre-ageing	Natural ageing	Pre-straining	Paint-baking
CS	-	-	-	-	-	-
H	10 h heating 450 °C / 10 h 7 h heating 520 °C / 10 h	-	-	-	-	-
PA		520 °C / 10 min Water quenching	100 °C / 5 h	-	-	-
NAPB			-	25 °C / 14 d	-	180 °C / 20 min
PANAPB			100 °C / 5 h		-	
PANA2%PSPB					2 %	
PANA5%PSPB					5 %	

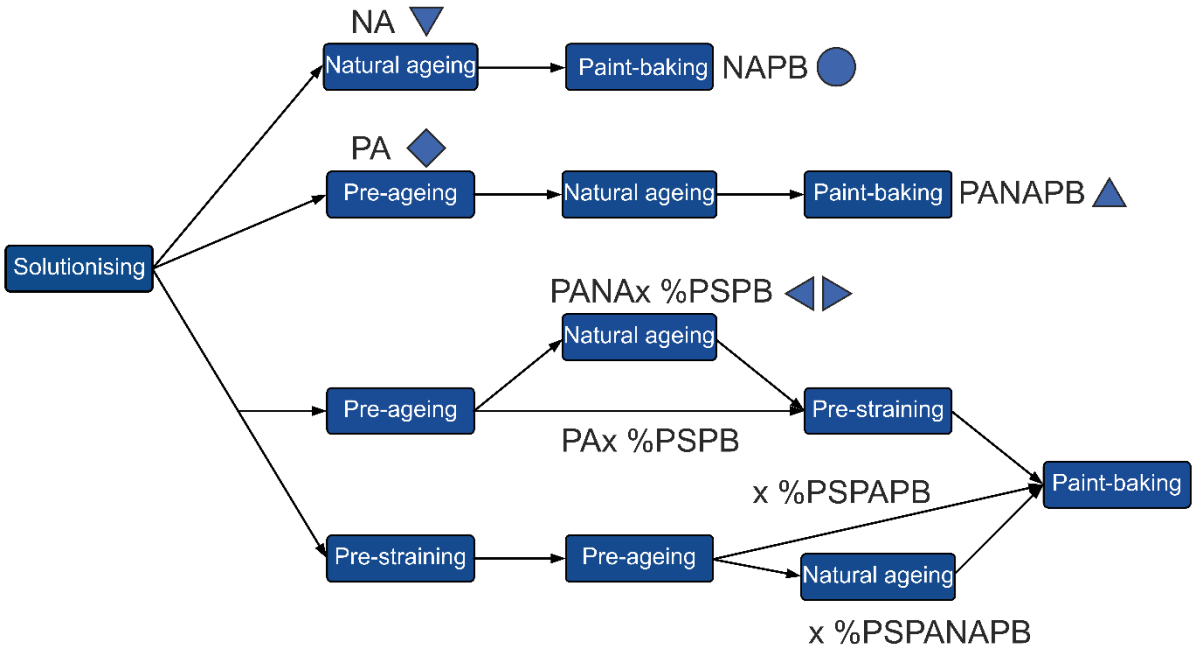

Supplementary Figure 1: Age hardening process. Schematic illustration of the heat treatment procedure with and without pre-deformation and symbols indicating the processing way in **Supplementary Figure 2**.

Supplementary Note 3: Results of tensile testing

Tensile testing was conducted for all alloys in the conditions described in **Supplementary Figure 1**. A general overview of the performance of the alloys compared to common automotive wrought and cast alloys is given in **Supplementary Figure 2**. **Supplementary Figure 3** thereby shows the results for the EU and EC-alloy in as-cast and homogenized conditions. **Supplementary Figure 4** – **Supplementary Figure 6** show the results of the tensile tests of the different alloys after processing and further determining the strain-hardening potential on hand of Kocks-Mecking plots.

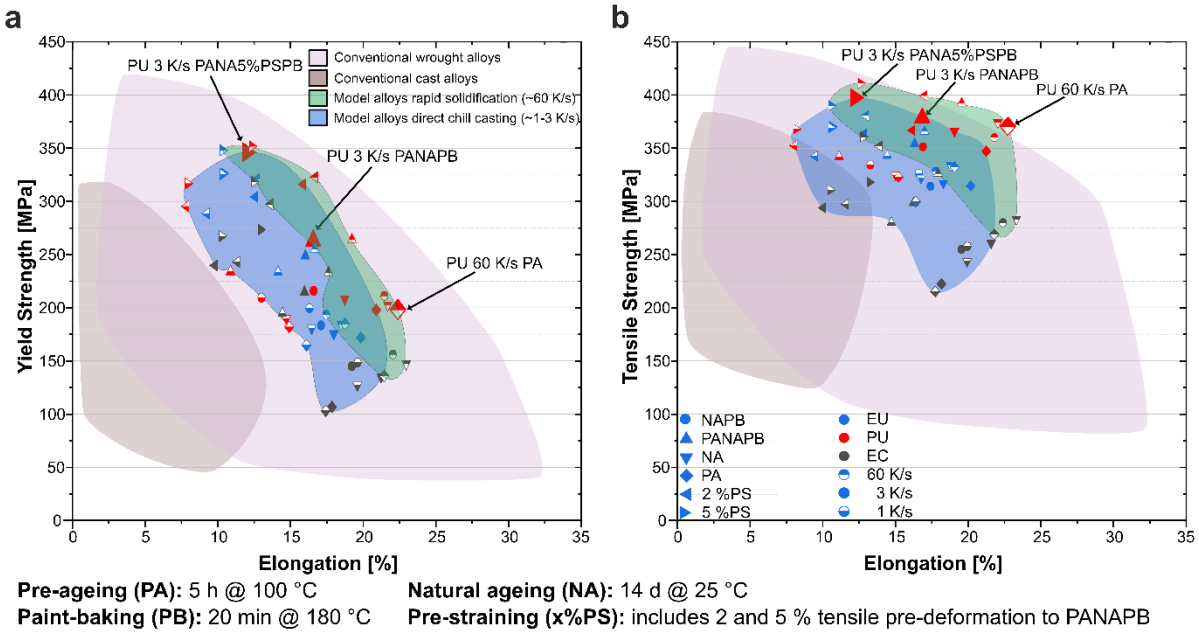

Supplementary Figure 2: Strength-ductility plot comparing today's commercial automotive alloys (wrought and cast alloys) from the literature to the investigated alloys. a Compares the yield-strengths to commercial alloys from literature [SR2]. **b** Compares the tensile strengths to commercial alloys. **a** and **b** include different cooling conditions (mimicking rapid solidification and direct chill casting)

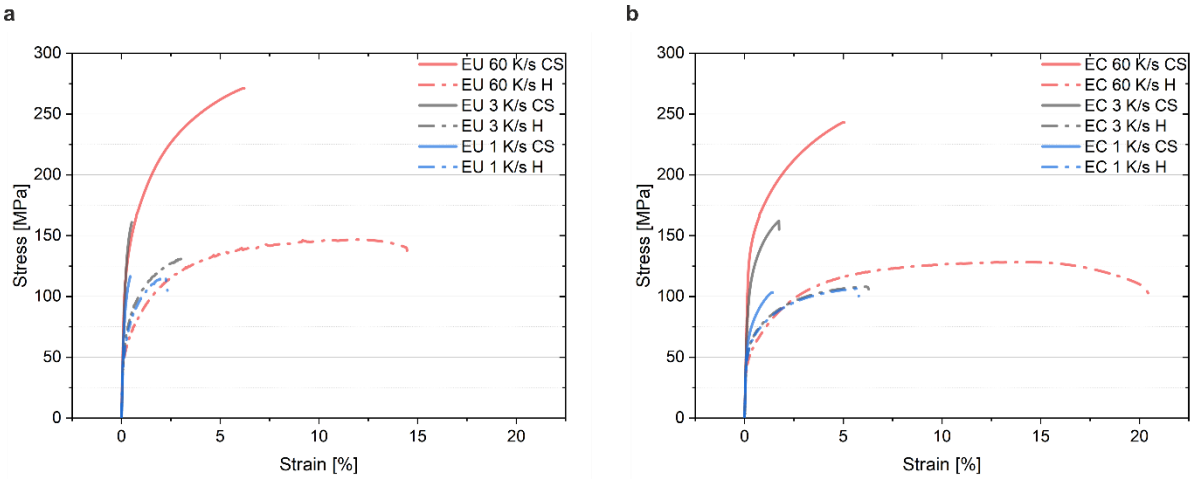

Supplementary Figure 3: Results of tensile tests in as-cast and homogenized conditions a All cooling rates for alloy EU ND. **b** All cooling rates for alloy EC ND.

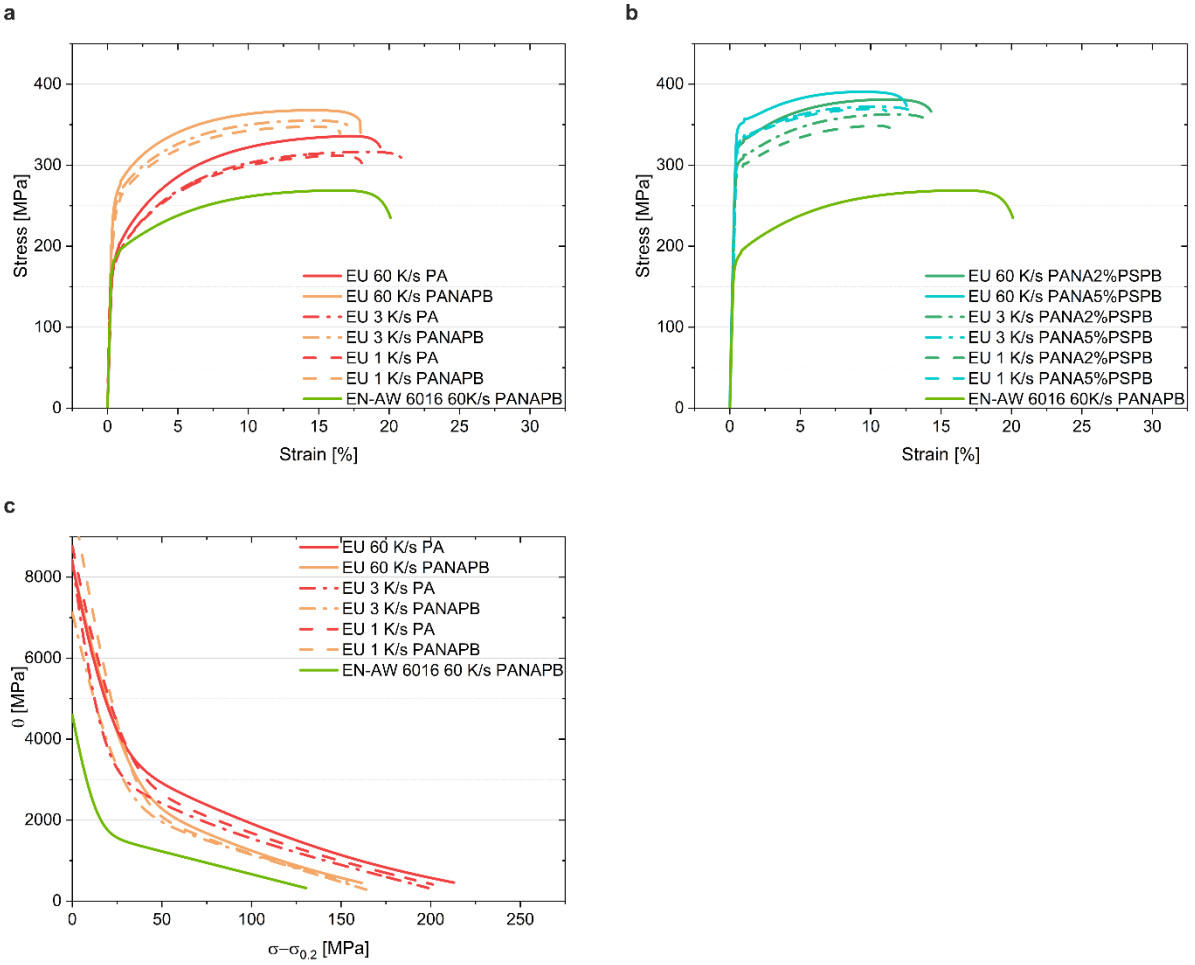

Supplementary Figure 4: Influence of heat treatments and pre-deformation on alloy EU ND for all cooling rates a Results of the tensile tests for processing routes without pre-deformation in comparison to common automotive sheet alloy 6016. **b** Results of the tensile tests for processing routes including pre-deformation in comparison to common automotive sheet alloy 6016. **c** Kocks-Mecking-plots of the processing routes without pre-

deformation showing higher strain-hardening potential than common automotive aluminium sheet alloy.

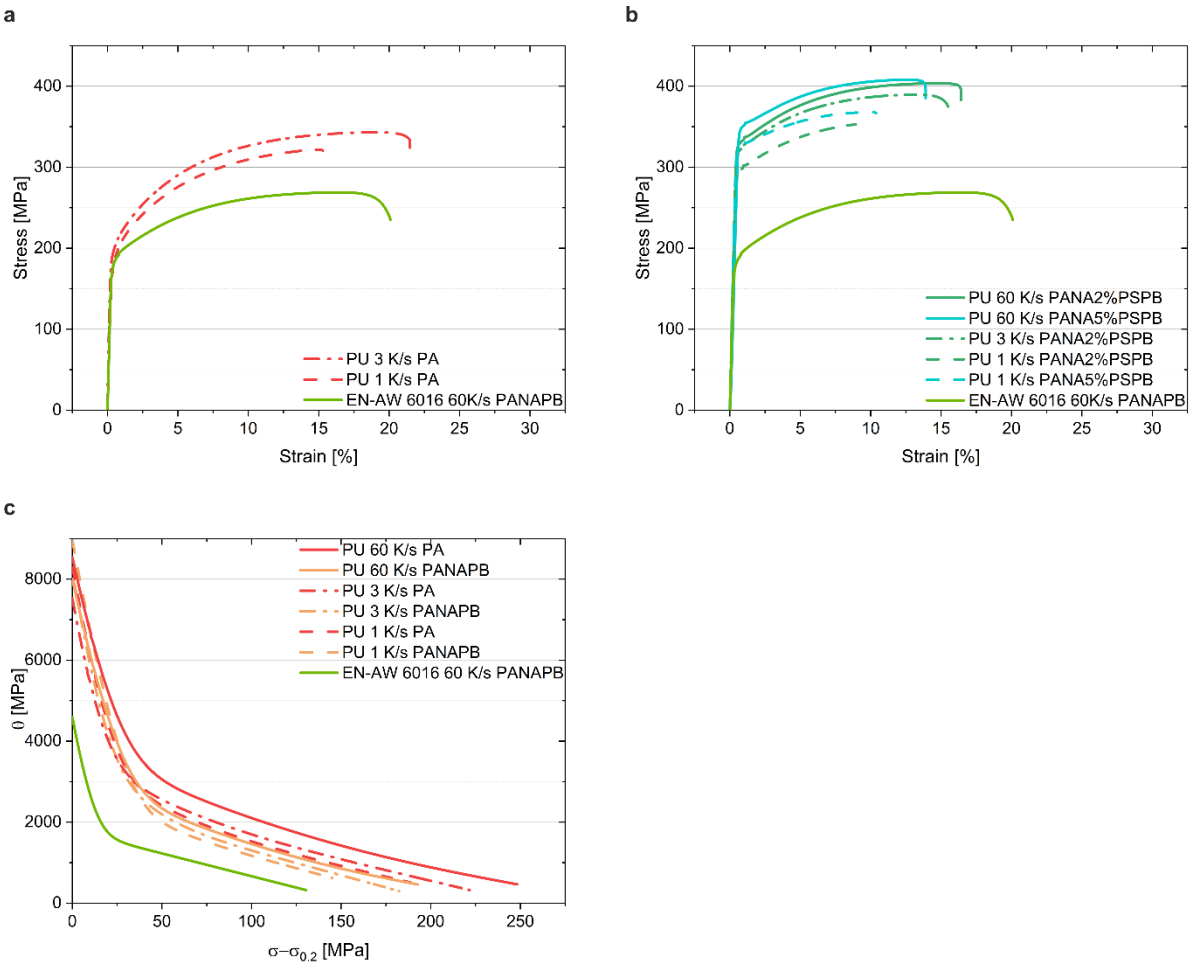

Supplementary Figure 5: Influence of heat treatments and pre-deformation on the remaining conditions of alloy PU ND for all cooling rates a Results of the tensile tests for processing routes without pre-deformation in comparison to common automotive sheet alloy 6016. **b** Results of the tensile tests for processing routes including pre-deformation in comparison to common automotive sheet alloy 6016. **c** Kocks-Mecking-plots of the processing routes without pre-deformation showing higher strain-hardening potential than common automotive aluminium sheet alloy.

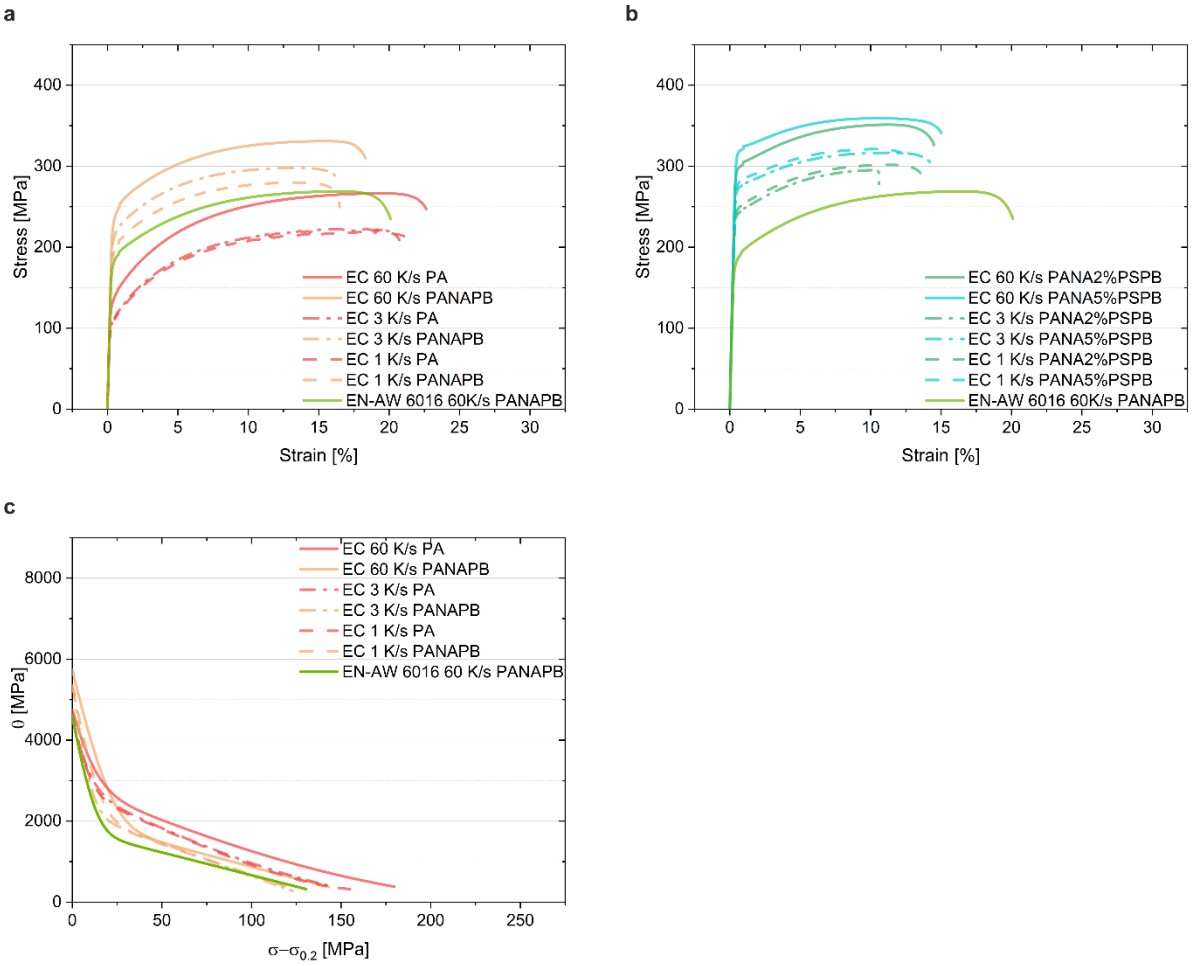

Supplementary Figure 6: Influence of heat treatments and pre-deformation on alloy EC ND for all cooling rate a Results of the tensile tests for processing routes without pre-deformation in comparison to common automotive sheet alloy 6016. **b** Results of the tensile tests for processing routes including pre-deformation in comparison to common automotive sheet alloy 6016. **c** Kocks-Mecking-plots of the processing routes without pre-deformation showing higher strain-hardening potential than common automotive aluminium sheet alloy.

Supplementary Note 4: Results of EBSD investigations

The microscopic investigations included SEM-micrographs of the PU-alloy in all cooling conditions after 5 % pre-straining. The EBSD-mappings (**Supplementary Figure 7**a-c) were measured after paint-baking, whilst KAM-mappings (**Supplementary Figure 7**d-f) were taken after deformation to uniform elongation. At a cooling rate of 1 K/s, grains larger than 40 µm are prevalent, whereas at 3 K/s, fewer large grains are observed in the material (**Supplementary Figure 7**a–c). In contrast, no grains exceeding 30 µm appear in the 60 K/s.

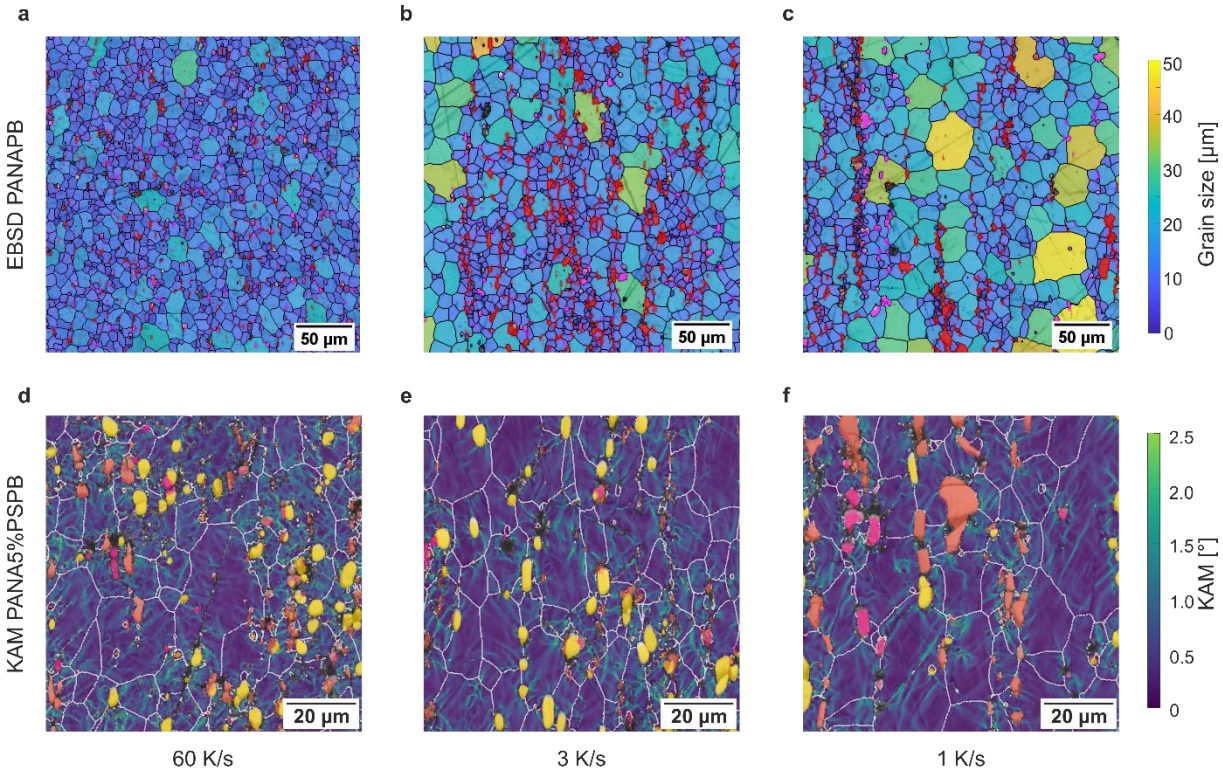

Supplementary Figure 7: Scanning electron microscopic investigation of the PU-alloy. a-c EBSD-mappings of the alloy PU alloy after pre-aging, natural aging and paint-bake treatment (PANAPB) following different cooling rates upon casting measured before deformation. **d-f** KAM-overlay maps of the PU alloy after pre-aging, natural aging, 5 % pre-straining and paint-bake treatment (PANA5%PSPB), following different cooling rates upon casting measured at the uniform elongation. Grain boundaries are marked in white, with Si-dominant IMPs in yellow, Fe-dominant IMPs in orange, and Mg-dominant IMPs in pink.

Supplementary Note 5: Results of APT analysis

After PA, more than 70 % of the detected clusters contain less than 33 atoms. In PANAPB this share is 53 % and 38 % in PANA5%PSPB. In contrast, 15 % contain more than 50 atoms after PA, while 36 % and 47 % do so for PANAPB and PANA5%PSPB respectively (see **Supplementary Figure 8**a). Regarding the Guinier-radius of the clusters and precipitates, 90 % are smaller than 2 nm in PA-condition, while for PANAPB and pre-strained states, almost 90 % have a Guinier-radius of 1–3 nm. It is conspicuous that the share of clusters and precipitates over 2 nm is larger in PANAPB than for pre-strained state (29 vs. 26 %). While the share of clusters/precipitates of more than 5 nm Guinier-radius is neglectable in PANAPB-material, in pre-strained condition it is at 2.2 % (see **Supplementary Figure 8**b). The median Guinier radii range from 1.26 nm in the PA state to 1.61 nm after 5% pre-straining. Chemically, both the paint-baking and the pre-straining processes generate higher median magnesium concentrations (Mg/(Mg+Cu+Si+Zn) of 0.38 and 0.37, respectively, compared to 0.31 in the PA condition) (**Supplementary Fig. 8**c). An overview of the cluster chemistry in different processing conditions is given by **Supplementary Table 3**.

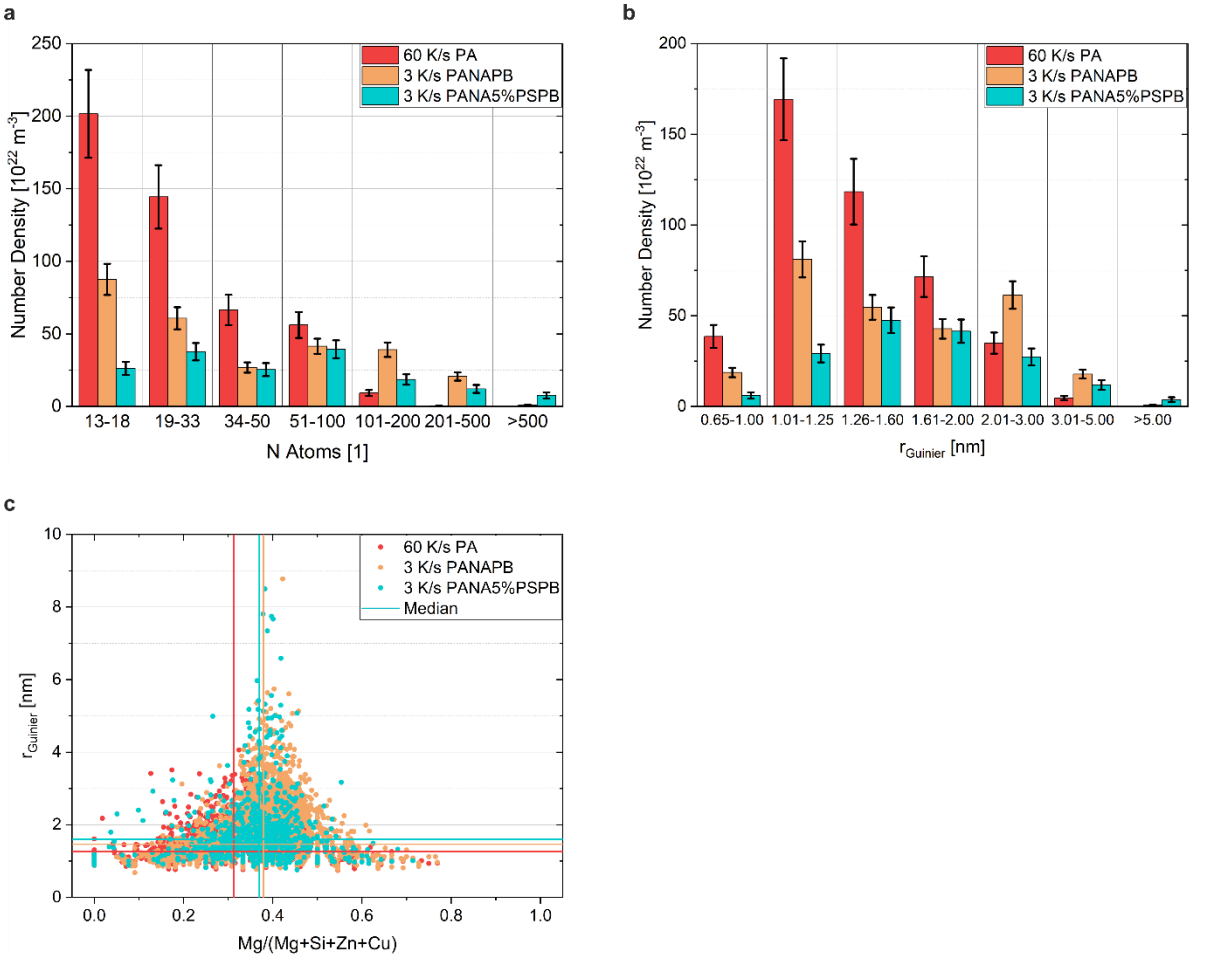

Supplementary Figure 8: Results of APT investigations for different processing conditions. a Number density of clusters and precipitates over their number of atoms for 60 K/s PA, 3 K/s PANAPB and 3 K/s PANA5 %PSPB. **b** Number density of clusters and precipitates over the Guinier-radius for 60 K/s PA, 3 K/s PANAPB and 3 K/s PANA5 %PSPB. **c** Guinier-radius in dependence of the Mg-ratio in clusters and precipitates for 60 K/s PA, 3 K/s PANAPB and 3 K/s PANA5 %PSPB.

Supplementary Table 3: Chemical analysis of the clusters and precipitates for different processing conditions.

Alloy	Composition	Mg	Zn	Cu	Si
PU 60 K/s PA	Overall [at-%]	0.60 ± 0.03	0.40 ± 0.03	0.52 ± 0.03	1.12 ± 0.03
	Matrix [at-%]	0.49 ± 0.03	0.40 ± 0.03	0.46 ± 0.02	0.98 ± 0.02
	Cluster/Precipitates [at-%]	2.22 ± 0.10	0.44 ± 0.06	1.29 ± 0.06	3.10 ± 0.06
	Solute [%]	24.58 ± 0.40	7.28 ± 0.64	16.55 ± 0.48	18.41 ± 0.21
	Volume fraction [%]	1.48			
PU 3 K/s PANAPB	Overall [at-%]	0.57 ± 0.02	0.37 ± 0.02	0.43 ± 0.02	1.01 ± 0.02
	Matrix [at-%]	0.37 ± 0.01	0.36 ± 0.02	0.37 ± 0.02	0.82 ± 0.01
	Cluster/Precipitates [at-%]	3.37 ± 0.06	0.43 ± 0.06	1.21 ± 0.06	3.65 ± 0.06
	Solute [%]	40.12 ± 0.24	8.01 ± 0.41	19.25 ± 0.30	24.69 ± 0.13
	Volume fraction [%]	2.34			
PU 3 K/s PANA5%PSPB	Overall [at-%]	0.59 ± 0.04	0.33 ± 0.04	0.47 ± 0.04	1.12 ± 0.04
	Matrix [at-%]	0.19 ± 0.02	0.32 ± 0.04	0.32 ± 0.03	0.73 ± 0.03
	Cluster/Precipitates [at-%]	3.54 ± 0.10	0.41 ± 0.11	1.57 ± 0.10	3.92 ± 0.10
	Solute [%]	72.21 ± 0.46	14.95 ± 0.89	40.34 ± 0.64	42.35 ± 0.24
	Volume fraction [%]	4.63			

Supplementary Note 6: TEM Investigation

TEM-investigations reveal low dislocation density in the 60 K/s PA-sample (**Supplementary Figure 9**a), and 3 K/s PANAPB material in **Supplementary Figure 9**b compared to the pre-strained material in **Fig. 3**h.

For the confirmation of the Q'-hardening precipitates, the diffraction pattern of the PANA5 %PSPB was analysed and reconstructed as shown in **Supplementary Figure 9**c and in literature [SR3].

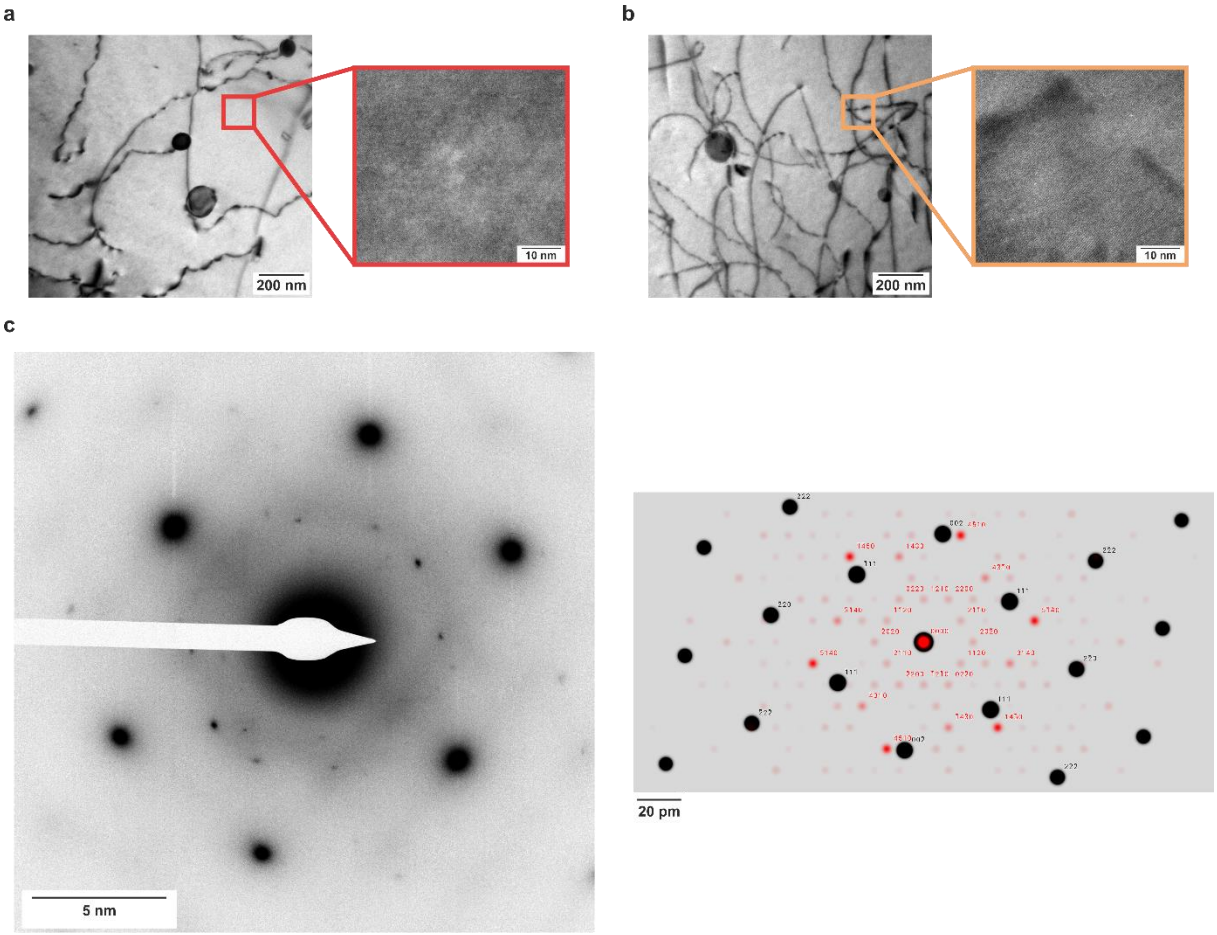

Supplementary Figure 9: TEM images showing interactions of dislocations and particles. (a) In the 60 K/s PA-material with high-resolution-insert. (b) For the 3 K/s PANAPB-sample with high-resolution-image inserted. **c** Diffraction pattern and indexing of the hardening precipitates in PANA5 %PSPB-material for confirmation of Q'-phase according to literature [SR3].

Supplementary Note 7: Simulation of vacancy concentration, dislocation density and diffusion ways during pre-straining

According to Militzer et al.[SR4] and Robson[SR5] we calculate the initial (c_0, equation **(1)**) and excess vacancy concentration c_{ex} with equation **(2)**. With the diffusion constant D (calculated according to **(3))** and a diffusion enhancement factor f (equation **(4))**, the diffusion paths can be determined by **(5)**. Equations **(2)** and **(5)** were thereby solved iteratively with an explicit integration scheme.

$$\boldsymbol{c_0 = 2.3 \cdot \exp\left(-\frac{H_V^f}{RT}\right)} \textbf{ (1)}$$

$$\boldsymbol{\frac{dc_{ex}}{dt} = \chi \frac{\sigma \Omega_0}{H_V^f} \dot{\varepsilon} - \left(\frac{D_V \rho}{\kappa^2} + \frac{D_V}{L^2}\right) c_{\mathrm{ex}}} \textbf{ (2)}$$

$$\boldsymbol{D_{Mg,Si,Cu} = D^0_{Mg,Si,Cu} \cdot \exp\left(-\frac{H^d_{Mg,Si,Cu} - H_V^f}{RT}\right)} \textbf{ (3)}$$

$$\boldsymbol{f = 1 + \frac{c_{ex}}{c_0}} \textbf{ (4)}$$

$$\boldsymbol{x^2_{Mg,Zn,Cu} = \int 4 \cdot f \cdot D_{Mg,Zn,Cu} \cdot dt} \textbf{ (5)}$$

The effective diffusion in dependence of vacancy concentration and pipe-diffusion along dislocation cores can be expressed by **(6)**. For the pipe-diffusion-coefficient D_p the activation energy for diffusion was assumed to be $0.55 \cdot H_j^d$ (activation energy for lattice diffusion)[SR5].

$$\boldsymbol{\mathrm{D}_{eff_{Mg,Si,Cu}} = D_{Mg,Si,Cu} \cdot \left(1 + \frac{c_{ex}}{c_0} + g \cdot \frac{D_{p_{Mg,Si,Cu}}}{D_{Mg,Si,Cu}}\right)} \textbf{ (6)} \text{ with } \boldsymbol{g = 2 \cdot \Omega_0 \cdot \frac{\rho}{b}}$$

The dislocation enhancement factor is defined as $\left(\boldsymbol{1 + \frac{c_{ex}}{c_0} + g \cdot \frac{D_{p_{Mg,Si,Cu}}}{D_{Mg,Si,Cu}}}\right)$.

$$\boldsymbol{c_0} = 2.3 \cdot exp\left(-\frac{64{,}000 \frac{J}{mol}}{8.314 \frac{J}{mol \cdot K} \cdot 373\ K}\right) = 2.51 \cdot 10^{-9} = \boldsymbol{2.51 \cdot 10^{-3}\ ppm}$$

$$\boldsymbol{\frac{c_{ex}}{c_0}} = \frac{2 \cdot 10^3 \text{ ppm}}{2.51 \cdot 10^{-3} \text{ ppm}} = \boldsymbol{8 \cdot 10^5}$$

$$\boldsymbol{g} = 2 \cdot 1.66 \cdot 10^{-29}\ \mathrm{m}^3 \cdot \frac{3 \cdot 10^{14}\ \mathrm{m}^{-2}}{2.86 \cdot 10^{-10}\ \mathrm{m}} = \boldsymbol{3.48 \cdot 10^{-5}}$$

As $\frac{c_{ex}}{c_0}$ and $\boldsymbol{g}$ are constant for Mg, Si and Cu, only the dislocation enhancement by dislocations (pipe-diffusion) has to be determined separately:

$$\boldsymbol{g} \cdot \frac{\boldsymbol{D_{p_{Mg}}}}{\boldsymbol{D_{Mg}}} = 3.48 \cdot 10^{-5} \cdot \frac{\mathrm{D}_{0_{\mathrm{Mg}}} \cdot \exp^{-\frac{0.55 \cdot 115{,}000 \frac{\mathrm{J}}{\mathrm{mol}}}{8.314 \frac{\mathrm{J}}{\mathrm{mol \cdot K}} \cdot 298\ \mathrm{K}}}}{\mathrm{D}_{0_{\mathrm{Mg}}} \cdot \exp^{-\frac{115{,}000 \frac{\mathrm{J}}{\mathrm{mol}}}{8.314 \frac{\mathrm{J}}{\mathrm{mol \cdot K}} \cdot 298\ \mathrm{K}}}} = \mathbf{4.09 \cdot 10^4}$$

$$\boldsymbol{g} \cdot \frac{\boldsymbol{D_{p_{Si}}}}{\boldsymbol{D_{Si}}} = \mathbf{1.46 \cdot 10^5}$$

$$\boldsymbol{g} \cdot \frac{\boldsymbol{D_{p_{Cu}}}}{\boldsymbol{D_{Cu}}} = \mathbf{1.55 \cdot 10^6}$$

The combined diffusion enhancement factor (excess vacancies and dislocations) results $8.41 \cdot 10^5$ for Mg, $9.46 \cdot 10^5$ for Si and $2.35 \cdot 10^6$ for Cu.

The results for the calculations are shown in Supplementary Figure 10, for a summary of the applied parameters see Supplementary Table 4.

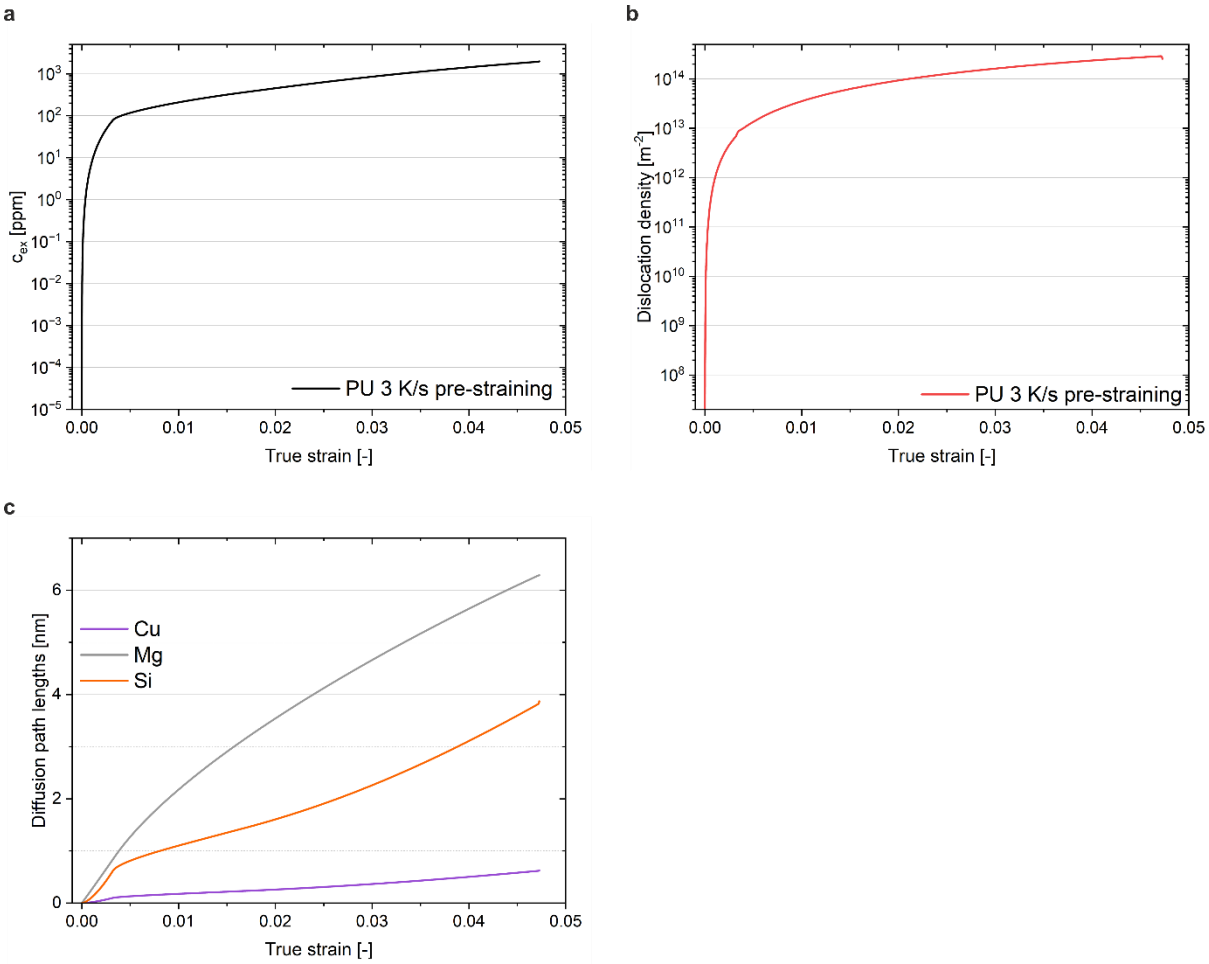

Supplementary Figure 10: Diffusion enhancement by pre-straining. a Introduction of excess vacancies during pre-deformation. **b** Increase of the dislocation density during pre-deformation resulting in more favourable nucleation places. **c** Extension of diffusion paths for Cu, Mg and Si through pre-straining.

Supplementary Table 4: Summary of the applied parameters for vacancy, dislocation density and diffusion path calculations.

Parameter	Notation	Value
Grain size–3 K/s	$d_{3\,K/s}$	~ 16 µm
Constant	α	0.3 [SR6]
Taylor factor	M	3.06 [SR6]
Shear modulus	G	25.4 GPa [SR6]
Burgers vector	b	$0.286 \cdot 10^{-9}$ m [SR6]
Fraction of external work stored by producing vacancies	χ	0.1 [SR4, SR5]
Atomic volume	Ω_0	$1.66 \cdot 10^{-29}$ m^3 [SR5]
Vacancy / self-diffusion enthalpy	H_V^{sd}	129 kJ·mol^{-1} [SR7]
Vacancy formation enthalpy	H_V^f	64 kJ·mol^{-1} [SR7]
Vacancy migration enthalpy	H_V^m	65 kJ·mol^{-1} [SR5]
Mg diffusion / Activation enthalpy	H_{Mg}^d	115 kJ·mol^{-1} [SR8]
Si diffusion / Activation enthalpy	H_{Zn}^d	122 kJ·mol^{-1} [SR9]
Cu diffusion / Activation enthalpy	H_{Cu}^d	135 kJ·mol^{-1} [SR9]
Pre-factor vacancy diffusion	D_V^0	$3 \cdot 10^{-5}$ m^2·s^{-1} [SR5]

Pre-factor Mg diffusion	D_{Mg}^{0}	$6.23 \cdot 10^{-6}$ m^2·s^{-1} [SR8]
Pre-factor Si diffusion	D_{Zn}^{0}	$1.19 \cdot 10^{-5}$ m^2·s^{-1} [SR9]
Pre-factor Cu diffusion	D_{Cu}^{0}	$6.47 \cdot 10^{-5}$ m^2·s^{-1} [SR9]
Dislocation arrangement	κ	1.0 [SR4]
Gas constant	R	8.314 J·mol^{-1}·K^{-1} [SR10]

Supplementary References

[SR1] Krall P., I. Weißensteiner and S. Pogatscher: Recycling aluminum alloys for the automotive industry: Breaking the source-sink paradigm. Resources, Conservation and Recycling, 202 (2024), 107370.

[SR2] Granta Design Limited: CES EduPack2023, Cambridge (2023).

[SR3] Arnberg L. et al.: The Crystal Structure of Al(x)Cu2Mg(12-x)Si7, (h-AlCuMgSi). Acta Chemica Scandinavica, 34a (1980), 1–5.

[SR4] Militzer M., W. P. Sun and J. J. Jonas: Modelling the effect of deformation-induced vacancies on segregation and precipitation. Acta Metallurgica et Materialia, 42 (1994), 133–141.

[SR5] Robson J. D.: Deformation Enhanced Diffusion in Aluminium Alloys. Metallurgical Transactions A, 51 (2020), 5401–5413.

[SR6] Cheng L. M. et al.: The influence of precipitation on the work-hardening behavior of the aluminum alloys AA6111 and AA7030. Metallurgical Transactions A, 34 (2003), 2473–2481.

[SR7] Mundy J. N.: Diffusion Mechanism in F.C.C. Metals. physica status solidi (b), 144 (1987), 233–241.

[SR8] Fujikawa S. and K. Hirano: Diffusion of 28Mg in aluminum. Materials Science and Engineering, 27 (1977), 25–33.

[SR9] Czerwinski F.: Thermal Stability of Aluminum Alloys. Materials (Basel, Switzerland), 13 (2020) online proceedings.

[SR10] Gottstein G.: Materialwissenschaft und Werkstofftechnik. Springer Berlin Heidelberg, Berlin, Heidelberg (2014).